Published in final edited form as:
J Mech Behav Biomed Mater. 2015 April ; 44: 96–108. doi:10.1016/j.jmbbm.2014.12.007.

High compressive pre-strains reduce the bending fatigue life of nitinol wire

Shikha Gupta[a], **Alan R. Pelton**[b], **Jason D. Weaver**[a], **Xiao-Yan Gong**[c], and **Srinidhi Nagaraja**[a,*]

[a]U.S. Food and Drug Administration, Center for Devices and Radiological Health, Office of Science and Engineering Laboratories, Division of Applied Mechanics, Silver Spring, MD, USA

[b]G. RAU Inc., Fremont, CA, USA

[c]Medical Implant Mechanics, Irvine, CA, USA

Abstract

Prior to implantation, Nitinol-based transcatheter endovascular devices are subject to a complex thermo-mechanical pre-strain associated with constraint onto a delivery catheter, device sterilization, and final deployment. Though such large thermo-mechanical excursions are known to impact the microstructural and mechanical properties of Nitinol, their effect on fatigue properties is still not well understood. The present study investigated the effects of large thermo-mechanical pre-strains on the fatigue of pseudoelastic Nitinol wire using fully reversed rotary bend fatigue (RBF) experiments. Electropolished Nitinol wires were subjected to a 0%, 8% or 10% bending pre-strain and RBF testing at 0.3−1.5% strain amplitudes for up to 10^8 cycles. The imposition of 8% or 10% bending prestrain resulted in residual set in the wire. Large pre-strains also significantly reduced the fatigue life of Nitinol wires below 0.8% strain amplitude. While 0% and 8% pre-strain wires exhibited distinct low-cycle and high-cycle fatigue regions, reaching run out at 10^8 cycles at 0.6% and 0.4% strain amplitude, respectively, 10% pre-strain wires continued to fracture at less than 10^5 cycles, even at 0.3% strain amplitude. Furthermore, over 70% fatigue cracks were found to initiate on the compressive pre-strain surface in pre-strained wires. In light of the texture-dependent tension−compression asymmetry in Nitinol, this reduction in fatigue life and preferential crack initiation in pre-strained wires is thought to be attributed to compressive pre-strain-induced plasticity and tensile residual stresses as well as the formation of martensite variants.

Despite differences in fatigue life, SEM revealed that the size, shape and morphology of the fatigue fracture surfaces were comparable across the pre-strain levels. Further, the mechanisms underlying fatigue were found to be similar; despite large differences in cycles to failure across strain amplitudes and pre-strain levels, cracks initiated from surface inclusions in nearly all wires. Compressive pre-strain-induced damage may accelerate such crack initiation, thereby reducing fatigue life. The results of the present study indicate that large compressive pre-strains are detrimental to the fatigue properties of Nitinol, and, taken together, the findings underscore the

*Correspondenceto:U.S.FoodandDrugAdministration,CenterforDevicesandRadiologicalHealth,10903NewHampshireAvenue, Building 62,Room2210,SilverSpring,MD20993-0002,USA.Tel.: +1 301 796 0396;fax: +301 796 9932. srinidhi.nagaraja@fda.hhs.gov (S. Nagaraja).

importance of accounting for thermo-mechanical history in the design and testing of wire-based percutaneous implants.

Keywords

Nitinol; Pseudoelastic; Shape memory; Fatigue; Bending; Crimp; Pre-strain; Endovascular

1. Introduction

Over the last decade, Nitinol, the nearly equiatomic metal alloy of nickel and titanium, has become a ubiquitous medical device material due to its unique shape memory and pseudoelastic material properties. These properties are attributed to a reversible martensitic transformation between the austenite and martensite phases, which may be temperature-induced (shape-memory) or stress-induced (pseudoelasticity). The parent austenite phase is an ordered B2 cubic lattice which is stable at high temperature while the lower symmetry martensite daughter phase possesses a B19' monoclinic crystal which is stable at lower temperatures. Conversion of the austenite phase to the martensite phase occurs via a diffusionless solid-to-solid phase transformation. This transition confers fully recoverable strains in excess of 6% to the material (Duerig et al., 1990; Shaw and Kyriakides, 1995), making Nitinol especially attractive as a material for percutaneous cardiovascular devices such as stent-grafts, vena cava filters and septal occluders (Duerig et al., 1999).

Endovascular implants are subjected to millions of cycles of multi-axial loading in vivo due to pulsatile blood flow and skeletal motions, making them susceptible to fatigue failure. Fatigue fracture of Nitinol endovascular devices remains a major concern, particularly in peripheral stents and septal occluders, where clinical fracture rates between 4% and 10% are still commonly reported (Fagan et al., 2009; Kay et al., 2004; Trabattoni et al., 2010). The fatigue properties of the Nitinol (NiTi) in intravascular devices is not just sensitive to material composition and processing (Launey et al., 2014; Matheus et al., 2011; Reinoehl et al., 2001; Schaffer and Plumley, 2009) but to the full thermo-mechanical history of the formed device. The thermo-mechanical history may include final shapesetting heat treatments/aging (Pelton et al., 2004; Pelton et al., 2003), and post-processing step such as loading onto a delivery system, sterilization, and final deployment (Duerig et al., 1999). Heat treatments have typically been used to optimize austenite finish temperature (A_f) and microstructural parameters (Pelton et al., 2000), and the effect of such treatments on the fatigue life of Nitinol devices has been studied over the past decade (Patel et al., 2006). In contrast, the effects of constraining the device onto a delivery system (crimping), sterilizing the device at high temperatures in this constrained state, and then releasing the constraint during deployment are still not well understood.

Crimp strains, or pre-strains, in endovascular devices may range from 4% to over 10%. For instance, Kleinstreur et al. reported maximum crimp strains of 8.86% and 10% for two different Nitinol materials in a diamond stent-graft model (Kleinstreuer et al., 2008). Similarly, pre-strains of 6−8% were calculated for different percutaneous heart valves (Kumar and Mathew, 2012). Though these pre-strains are largely recovered upon deployment, the material in the device has undergone a large forward and reverse mechanical strain excursion even before encountering any physiological deformation.

Similarly, sterilization imposes a thermal cycle on endovascular devices prior to deployment. Constraining onto the delivery system, such as a catheter, is often performed at low temperatures near or below the martensite finish temperature (M_f) The constrained device may then be sterilized at temperatures above A_f, stored at ambient temperature before implantation, and finally exposed to body temperatures just prior to deployment/release.

Irrespective of whether it results in a permanent set, this single large thermo-mechanical strain cycle can alter the material microstructure through the accumulation of dislocations, interface formation and the persistence of martensite nuclei within the austenite matrix (Brinson et al., 2004; Pelton, 2011; Pelton et al., 2012). Such changes may manifest as shifts in phase transition temperatures, plateau stresses and transformation strains (Gong et al., 2002; Henderson et al., 2011; Miyazaki et al., 1986; Urbina et al., 2009), and as a result, may alter the fatigue behavior of the material. Designing Nitinol devices against fatigue fracture not only demands an understanding of in-service loads, but of how the device's complex thermo-mechanical history affects its material level fatigue behavior. While numerous computational (Grujicic et al., 2012; Kumar et al., 2013; Rebelo et al., 2009) and some experimental studies (Pelton, 2011; Pelton et al., 2008) of device-level fatigue have incorporated crimping and deployment into the investigational protocol, few studies have clearly examined how this pre-strain cycle impacts overall fatigue properties. Schlun et al. subjected pseudoelastic NiTi to an 8% tensile pre-strain and examined the evolution of the cyclic strain−stress behavior at 0.2% and 1.2% strain amplitude and 2% mean strain for 100 cycles (Schlun et al., 2011). The authors observed hysteresis and permanent set in the stress −strain curve at 1.2% strain amplitude over 100 cycles but the curve remained constant at 0.2% strain amplitude. However, they did not elucidate the impact of the initial 8% pre-strain on these findings. More recently, Pelton et al. investigated the fatigue behavior of different compositions of Nitinol wire at large strain amplitudes (5−10%) and found the wires fractured in less than 10^3 cycles (Pelton et al., 2013). Though such strain amplitudes exceed physiologic loading conditions, the results suggest that even a single strain excursion at such high strains may consume a measurable portion of the fatigue life of the material.

Bending is one of the predominant loading modes in many wire-based endovascular devices (Berg, 1995; Wick et al., 2005). As the fatigue life of pseudoelastic Nitinol is strain-controlled, rotary bend testing, which provides a simple method for strain-controlled materials characterization of wires, has been employed extensively over the past decade to investigate the fatigue behavior of medical grade Nitinol. The technique has been used to successfully examine the effects of material composition and processing (Reinoehl et al., 2001), specimen geometry (Norwich and Fasching, 2009) and surface finish on fatigue life of wires (Patel and Gordon, 2008). Therefore, the objective of the present study is to investigate the effect of high bending pre-strain on the low- and high-cycle fatigue properties of pseudoelastic Nitinol wire using rotary bend testing (RBT).

2. Methods

2.1. Nitinol wire

All testing was conducted on 0.5 mm diameter electropolished $Ni_{50.8}Ti_{49.2}$ Nitinol wire (Nitinol Devices and Components, Fremont, CA) that conforms to ASTM F2063. The wires were drawn with approximately 45% cold work and then straightened by conventional means (Pelton et al., 2000). The wires were then thermally treated (500 °C/3 min) to achieve an A_f of 15±3 °C, typical of implantable devices, as measured by bend free recovery (ASTM F2082, 2006). The wires were subsequently electropolished in an nitric acid−methanol solution at temperatures less than −50 °C. Fig. 1 shows the uniaxial tensile curve from a representative wire tested at 37 °C per ASTM F2516 at 0.5 mm/min. The wires exhibited an upper plateau stress of 650 MPa, lower plateau stress of 366 MPa and an elongation at fracture of 12.1%.

2.2. Thermo-mechanical pre-strain

Pre-strained wires were subjected to either 8% or 10% bending pre-strain. The pre-strain procedure was designed to mimic the thermo-mechanical history to which the wire would be subject prior to in-vivo loading, including loading onto a delivery device (crimping), sterilization and deployment. To simulate crimping, each wire sample was secured on each end with screws onto either 6.25 mm (maximum 8% prestrain) or 5 mm (maximum 10% pre-strain) fixed diameter Delrin mandrels, and both wire and mandrel were placed in a 0 °C ice bath for 2 min. Each wire was wrapped around the mandrel while immersed in the ice bath. To simulate ethylene oxide sterilization, the wrapped wire was subsequently submerged in a 60 °C bath for 2 min, followed by a room temperature soak for 2 min (Fig. 2). The two-minute duration at each pre-strain step was deemed sufficient since time is not a factor in martensitic transformations or in plasticity at such low temperatures.[1] Before the wire was uncoiled to release the pre-strain, a marker was used to identify the outer (tensile) pre-strained surface. Control (0% pre-strain) wires were subject to the same thermal history, but were left unconstrained in each bath. All samples were stored at room temperature until testing.

2.3. Residual strain

To quantify the extent of permanent set in the pre-strained wires, two 8% and two 10% wires were subjected to the pre-strain protocol. Each wire was imaged with a digital camera (Nikon D90) before and after heating to 200 °C, above the martensite deformation temperature, M_d, for 5 min in an oven (Carbolite CWF 12/13). ImageJ was used to approximate residual strain at 22−25 points along the length of the wire. An ‘instantaneous’ radius of curvature was estimated by calculating the radius of a circle composed of three adjacent points, approximately 8−10 mm apart, taken along the wire length. From the radius of curvature at each point, Eq. (1) was used to estimate the instantaneous residual strains along the wire length and compute an average permanent set.

[1]Nitinol creep has been extensively studied at temperatures ranging from ~500 °C to 1100 °C and with stress values from ~5 to 180 MPa (Oppenheimer et al., 2007 and references therein). Based on these data and experience of the authors Nitinol is not affected by time under stress conditions at homologous temperatures less than~0.4Tm.

2.4. Rotary beam fatigue tests

Fully reversed ($\varepsilon_{min}/\varepsilon_{max} = -1$) rotating bend fatigue tests were performed using modified Valley Instruments (Positool Technologies) rotary beam fatigue testers. To mimic physiologic conditions, and minimize possible adiabatic effects, tests were conducted in a 37 °C temperature-controlled circulating water bath at six different strain amplitudes: 0.3%, 0.4%, 0.6%, 0.8%, 1.0%, 1.2% and 1.5%. Square Delrin blocks machined with a 1.5 mm wide semi-circular mandrel groove were incorporated into the test apparatus to enable guided rotary beam testing, ensuring a more uniform strain along the length of the wire and mitigating potential vibratory motions (Norwich, 2014; Weaver et al., 2013). The radius of each mandrel groove was determined by the strain amplitude according to the following equation:

$$\varepsilon_a = \frac{d}{2R}$$

where d is the diameter of the wire, R is the radius of the mandrel, and ε_a is the strain amplitude. During testing, one end of the wire was clamped in a motor-driven chuck. The remaining length of the wire was inserted into the semi-circular groove, with the opposite end of the wire rotating freely outside the groove (Fig. 3). Wire guides prevented excessive motion of the free end. The chuck rotated at a constant frequency of 3600 RPM (60 Hz), with the strained wire experiencing an alternating state of tension and compression with each rotation. Fifteen to eighteen samples were evaluated at each strain amplitude; n=5−6 for each pre-strain (Table 1).

To date, nearly all RBF studies of Nitinol have been conducted at cyclic strains of 0.4% or greater to 10^7 cycles or less, which approximates a 10-year duration of in vivo musculoskeletal motions such as walking and stair climbing (Nikanorov et al., 2008). However, FDA guidelines for endovascular devices such as stents also recommend durability tests to simulate cardiac cyclic deformation under relevant pulsatile loading for approximately $4{\times}0^8$ cycles. Though run out values at 10^7 cycles are routinely deemed as the fatigue limit of the material, it remains unclear whether these values are representative of the strain limit at higher cycles. To ascertain whether the fatigue strain limit at 10^7 may be effectively extrapolated to higher cycles, the wire samples in the present study were cycled until fracture or until the cycle count reached 10^8 cycles.

2.5. Fractography

Fractured surfaces were examined with scanning electron microscopy (SEM, JEOL JSM-6390LV) to characterize crack-initiation and propagation features. Images were acquired at 20 kV with 30 mm spot size and 12 mm working distance. The location of crack-initiation relative to the regions of tensile and compressive pre-strain was also identified in wires subject to 8% and 10% pre-strains. SEM images were further analyzed to estimate the relative size of the fatigue crack growth region. An open source image processing software (National Institutes of Health ImageJ) was used to measure the crack growth area, defined as the ratio of the stable fatigue crack growth area to the entire fracture surface area. This analysis program was further used to measure the crack shape, defined as the ratio of the maximum crack length (a_{max}) to the maximum crack width ($2b_{max}$) of the area of stable crack growth. In addition, surface features along the circumferential surface of the wires were imaged via SEM and backscatter electron imaging (BEI).

2.6. Statistics

One-way ANOVA with Tukey's post-hoc tests were used to assess differences between pre-strain groups at fixed strain amplitude and between alternating strain levels for a given pre-strain. All data were presented as mean±SD. *P*-values less than 0.05 were considered significant.

3. Results

3.1. Retained martensite vs plasticity

Residual set was observed in all samples that were exposed to 8% or 10% pre-strain (Fig. 4). In the four wires in which remnant set was analyzed before and after heating above M_d, the average set across the length of the wire was less 0.1% (Table 2). Further, the set in the 10% pre-strain wires was significantly ($p<0.05$) greater than that measured in the 8% pre-strain wires. Though a reduction in average remnant strain was noted for all samples after heating above M_d, the change was not significant due to the large spatial variation in residual set observed across the length of the wires. A permanent set of approximately 0.023% and 0.057% remained in the 8% and 10% pre-strain wires, respectively, after heating.

3.2. Fatigue cycling

Rotary bend fatigue testing revealed that the strain life of the Nitinol wires decreased with increasing strain amplitude, irrespective of pre-strain level (Fig. 5). Two distinct fatigue regions were observed − a low-cycle regime ($\leq 5\times10^4$ cycles) and a high-cycle fatigue regime. Above 0.8% strain amplitude, the fatigue life of all samples was less than 10^5 cycles, and there were no significant differences in cycles to failure between pre-strain groups. For the 0% and 8% pre-strain levels, the strain life curve in the low cycle region (0.8−1.5% strain amplitude) could also be modeled with an empirical power−law relationship with a power−law exponent of −0.36 and −038, respectively.

At 0.8% strain amplitude and below, fatigue life of the pre-strained wires diverged. At 0.8% strain amplitude, the average strain life of 10% pre-strain wires ($1.45\pm0.2\times 10^4$ cycles) was lower ($p<0.001$) than 0% ($2.4\pm0.4\times10$ cycles) and 8% ($2.3\pm0.2\times0$ cycles) pre-strain wires, while both 8% and 10% wires had significantly reduced fatigue resistance compared to 0% pre-strain wires at 0.6% strain amplitude ($p<0.0001$). At least one sample in the control and 8% prestrained samples reached runout at 0.6% and 0.4% strain amplitudes, respectively, at both 10^7 and 10^8 cycles. At 0.4% ε_a, all five 0% pre-strain wires and four of five 8% pre-strain wires withstood 10^8 cycles of bending. In contrast, all 10% pre-strain wires fractured in the low-cycle region at less than 10^5 cycles, even at 0.3% strain amplitude.

3.3. Fractography

Despite the differences in fatigue life and residual set, the morphology of the fracture surfaces was similar between prestrain groups at larger strain amplitudes (Fig. 6(a-c)) and lower strain amplitudes (Fig. 6(d-f)). Each fracture surface consisted of two distinct regions: a thumbnail shaped region of crack initiation and fatigue crack growth (Fig. 7a) followed by an overload region of ductile tensile fracture (Fig. 7b).

Cracks were found to nucleate from surface inclusions in the region of stable crack growth, though individual fatigue striations could not be perceived (Fig. 7c). The region of tensile overload was comprised of characteristic ductile dimples and voids.

With respect to the relative area of the two regions, at each pre-strain level, the crack growth area increased significantly (p<0.05) with decreasing strain amplitude (Fig. 8a), varying from approximately 24% to 55% at 1.5% and 0.6% strain amplitudes, respectively. For fixed strain amplitude however, the average crack growth area was statistically similar between pre-strain levels, and, like surface morphology, was comparable even in wires with vastly different fatigue cycles. For example, a 0% pre-strain wire that fractured at 12 M cycles and an 8% pre-strain wire that fractured at 45k M cycles at 0.6% strain amplitude both had a crack growth area of 55%. Similarly, crack shape ($a_{max}/2b_{max}$) was also comparable between different pre-strain levels at all strain amplitudes. In contrast to crack growth area, however, its value was largely independent of alternating strain level (Fig. 8b). For strain amplitudes between 0.8% and 1.5%, the average value of $a_{max}/2b_{max}$ was approximately 2.1 for all three pre-strain levels. Only at 0.6% strain amplitude, where the crack growth front shifts from a thumbnail shape to a more linear shape, did $a_{max}/2b_{max}$ drop significantly (p<0.0001).

Within the crack initiation region, cracks were observed to preferentially initiate from the compressive pre-strain surface. In more than 70% of the 8% and 10% pre-strain wires, fatigue cracks started from inclusions within ±45° from the location of maximum compressive bending strain (Table 3). Irrespective of the relative location of crack initiation, there was no evidence of microcrack coalescence around the circumferential periphery of the fracture surface. Though the microcracks observed along the longitudinal surface of the wires also originated from voids associated with surface inclusions (Fig. 9), the number of microcracks was insufficient to quantify microcrack density or to compare differences along the compressive and tensile surface.

4. Discussion

The present work examined the fatigue behavior of pseudoelastic Nitinol wires subject to pre-strains that simulated crimping, sterilization and deployment of transcatheter devices. Zero mean strain rotary bend fatigue testing was used to quantify the fatigue life of wires subject to 0%, 8% and 10% bending prestrain over a range of strain amplitudes. The imposition of an 8% and 10% pre-strain resulted in pronounced residual set in the wires, particularly at 10% pre-strain. Though no discernible differences in fatigue life were observed between control and pre-strain samples at higher strain amplitudes (≥1.0% ε_a), large bending pre-strains significantly reduced the fatigue properties of Nitinol wire at low strain amplitudes, with the 10% pre-strain having a more deleterious impact. Furthermore, over 70% of the wires subject to a pre-strain experienced crack initiation from the region of compressive strain. These observations of reduced high-cycle fatigue performance and preferential compressive crack initiation with high bending pre-strain may be attributed to two simultaneous factors: effects of plasticity and effects of martensite variants. We will first address these effects in the context of the pre-strain process, and then discuss our fatigue and fractography findings.

4.1. Effects of bending pre-strain − plasticity

The crystallographic texture in Nitinol is highly dependent on product form (Robertson et al., 2006), and due to the drawing process, wires develop a strong texture in the drawing direction. Nitinol wires typically possess a ⟨111⟩ texture, which more readily accommodates tension than compression in the drawing direction (Gall et al., 1999). While the nominal elastic modulus in tension and compression is similar, in general the compressive stress −strain curves exhibit higher plateau stresses (more difficult to form martensite), steeper transformation slopes (“work hardening”), and lower recoverable transformation strains (greater plasticity) than in tension (Jacobus et al., 1996; Plietsch and Ehrlich, 1997). Given this tension−compression asymmetry, to understand the results from the bending pre-strain process, it is necessary to consider how these prestrains, and therefore the resultant stresses, partition across the diameter of the bent wires. Bending produces a localized strain (stress) gradient across the diameter of the wire, with the highest strains (stresses) concentrated along outer fibers of the wire (Reedlunn et al., 2014; Wick et al., 2005). For the present purposes, it is beneficial to consider the stress distribution across the wire diameter. Fig. 10a (after (Bannantine et al., 1990)) is a schematic illustration of the stress distribution across the Nitinol wire during the pre-straining process which takes into account its well-known tension−compression asymmetry (Gall and Sehitoglu, 1999; Gall et al., 1999). There are elastic stresses on both sides of the neutral axis that transition to stress-induced martensite whereby the tension stress plateau is longer and forms at a lower stress value than on the compression side. In the outer regions, where the greatest strains are reached, the surface stresses on the compression side are greater than those on the tension side. There is plasticity within both the tension and compression regions that results in dislocation generation.

Reedlunn et al. (2014) tested pseudoelastic Nitinol tubes (A_f 19 °C) in tension, compression, and pure bending at room temperature with custom-designed fixturing and stereo digital image correlation to quantify the local surface strain field. They observed localized propagating transformation fronts in uniaxial tension, but not in uniaxial compression. Similarly, the strain fields in bending contained localized strain on the tensile side, but no such localizations on the compression side of the tube. They presented an elegant strain-based model that considers preferred bending kinematics and localized kinematics to explain their observations of localized strain asymmetries. They simulated the bending moment−curvature response up to the end of the loading plateau based on their uniaxial data. However, their bending strains did not reach the 8−10% range and therefore did not incorporate effects of plasticity that would result in such an extreme permanent set as was observed in the current testing.

In a recent neutron diffraction study, Stebner et al. (2013) investigated the contributions to strain under uniaxial tension−compression of thermal martensite to ±18%. They attributed the tension−compression asymmetry to strain partitioning according to the following relationship:

$$\Delta\varepsilon^{\text{total}} = \Delta\varepsilon^{\text{elastic}} + \Delta\varepsilon^{\text{accommodation twinning}} + \Delta\varepsilon^{\text{deformation twinning}} + \Delta\varepsilon^{\text{slip}}$$

where the total strain ($\Delta\varepsilon^{total}$) is partitioned into elastic strain ($\Delta\varepsilon^{elastic}$), two contributions from twinning ($\Delta\varepsilon^{accommodation}$ and $\Delta\varepsilon^{deformation}$) and plasticity ($\Delta\varepsilon^{slip}$)[2]. Based on results from a follow-up investigation of pseudoelastic Nitinol (A. Stebner, S. Clausen, A. R. Pelton, in process 2014), the amount of plastic strain contribution from the bending pre-strain in the present study is comparable to that observed in thermal martensite (Barney et al., 2011; Stebner et al., 2013). Therefore, approximately 17% of the tensile strain and 34% of the compressive strain can be attributed to $\Delta\varepsilon^{slip}$ in the outer fibers for the 8% pre-strain conditions. $\Delta\varepsilon^{slip}$ contributions increase to 29% and 43%, respectively, for tension and compression, during 10% pre-strain. Note that slip is a more significant contributor to the compressive response at both levels of pre-strain. Consequently, the compression side of the wires will have greater plasticity at both levels of pre-strain. Furthermore, the corresponding stress at the 8 and 10% pre-strain is also proportionally greater in compression than in tension, and is reflected in the schematic diagram in Fig. 10a. The result of this prestrain deformation is that the outer fibers on both the tension and compression sides will contain a high level of dislocations with a greater amount on the compression side. Consequently, this asymmetry will also be manifest as greater macroscopic damage accumulation on the compressive surface (Chinubhai et al., 2013; James et al., 2004). It is expected that the amount of plasticity increases as the pre-strain increases from 8% to 10%.

During exposure to 60 °C temperatures with the wires still wrapped around the mandrels (to simulate EtO sterilization), the tensile and compressive stresses increase by the well-known Clausius Clapeyron relationship (Shimizu and Tadaki, 1984), resulting in greater local strains with concomitant additional plasticity. Upon removal from the constraint, both tensile and compressive residual stresses must be present in order to satisfy all equations of internal force and moment equilibrium, ΣF=ΣM=0. Therefore, the surface regions that were plastically deformed prevent the adjacent elastic (and pseudoelastic) regions from undergoing complete elastic recovery to the unstrained condition. As such, the elastically (and pseudoelastically) deformed regions on the tensile side are left in residual tension and the regions that were plastically deformed must be in the state of residual compression to balance the stresses over the cross section of the wires. Conversely, the elastically (and pseudoelastically) deformed regions on the compression side are left in residual compression; the regions that were plastically deformed on the compression side will have a tensile residual when the constraints are removed. Furthermore, due to the tension −compression stress asymmetry in Nitinol, the depth of the tensile residual stress is likely greater than on the compressive residual stress. A possible stress redistribution for the unconstrained wires is schematically shown in Fig. 10b.

[2]For the present case of wire deformation above the Af temperature, it is expected the that strain partitions as follows: $\Delta\varepsilon^{total} = \Delta\varepsilon^{elastic} + \Delta\varepsilon^{transformation} + \Delta\varepsilon^{slip}$ (Barney, Xu et al. 2011)

4.2. Effects of bending pre-strain − martensite formation

In addition to plastic deformation during the pre-strain process, the wires also undergo transformation from austenite to martensite as the stresses reach sufficient level across the diameter (see Fig. 10a). As such, there will be a gradient of volume fraction of martensite from the elastic regions to the outer surfaces. The greatest volume fraction of martensite therefore coincides with the greatest amount of plasticity at the outer surfaces. The dislocations will interact with the martensite so that these microstructures will consist of deformed martensite and dislocations, even after unloading (Otsuka and Ren, 2005; Stebner et al., 2013). However, different variants of martensite form through the wire cross section during the pre-straining operation in response to the local stress state and texture of the wires. Stebner et al. (2013) demonstrated that the material prefers axial orientation alignments near[3],[4] $(010)_M$ in tension and $(100)_M$ in compression. According to phenomenological theory $(010)_M$derives from $(01\bar{1})_{B2}$ and $(100)_M$ derives from $(\bar{1}00)_{B2}$ (Matsumoto et al., 1987). Austenite grains with orientations near $\{011\}_{B2}$ have a lower transformational free energy with recovery strains of approximately a factor of three greater than those near $\{100\}_{B2}$ (Bhattacharya, 2003; Miyazaki et al., 1984). Consequently, the martensite that forms on the tension side may more readily transform back to austenite upon unconstraining even though it resides in a compressive residual stress field. In contrast, it is more difficult to transform martensite from the compression side in its tensile residual stress field, thereby leaving greater retained deformed martensite on the compressive surface.

4.3. Fatigue cycling

Fully reversed rotary bend fatigue testing was performed on the 0%, 8% and 10% bending pre-strain at strain amplitudes ranging from 0.3% to 1.5%. The strain life curve exhibited a characteristic low-cycle fatigue region in which fatigue life increased sharply with decreasing strain amplitude. For 0% and 8% pre-strain wires this region could be modeled as a power law with an exponent of −0.36 and 0.38, respectively. A nearly flat high-cycle fatigue region (for $N_f>10^5$) was also observed in 0% and 8% pre-strain wires, with a run out at 10^8 cycles between 0.4% and 0.6% strain amplitudes.

Distinct cyclic deformation mechanisms underlie the low-and high-cycle fatigue regions; in the low-cycle region, the material accommodates strain in each cycle via elastic deformation and stress-induced martensite formation, while elastic deformations dominate in the high-cycle region. The transition between the two regions typically occurs at the initial transformation strain (approximated from a uniaxial tensile test, see Fig. 1), which is a function of composition, processing, thermo-mechanical history and test temperature. These factors further impact how quickly a fatigue limit is reached once the material transitions into the high-cycle region (slope of the high-cycle $\varepsilon_a - N_f$ curve). Therefore, the fatigue properties observed herein are expected to be congruous with those reported in previous high-cycle RBF studies of similarly processed pseudoelastic Nitinol wire examined under comparable test conditions. For instance, Pelton and colleagues recently conducted RBF

[3] Specifically, the dominant martensite orientations $(150)_M$ in tension and $\langle 322 \rangle_M$ in compression.

[4] More recent studies by Stebner et al. (A. Stebner, S. Clausen, A. R. Pelton, in process 2014) show that the martensite formed in tension and compression of pseudoelastic Nitinol is comparable to that formed from the thermal martensite at the higher strains.

testing of 0.6 mm $Ni_{50.8}Ti_{49.2}$ wires with a bright or dark surface and an A_f between 2 and 4 °C (Pelton et al., 2013). The wires were tested at −25 °C, 23 °C and 60 °C at strain amplitudes ranging from 0.6%−10%. At 23 °C, which corresponds to the same ΔT (Test temperature − A_f) as the present study, they reported similar values for cycles to failure in the low- and high-cycle fatigue regime as those observed for 0% pre-strain wires. The transition from the low-cycle regime also occurred at 0.8% strain amplitude (initial transformation strain) and the slope of the best-fit log-log strain life curve for strain amplitudes between 0.8% and 2% was 0.33 and 0.32 for the bright and dark surfaces, respectively. They also observed run out at 10^7 cycles at 0.6% strain amplitude. In earlier work, Sheriff et al. and Reinoehl et al. also investigated the RBF behavior of pseudoelastic $Ni_{50.8}Ti_{49.2}$ wires (Reinoehl et al., 2001; Sheriff et al., 2005). Based on the extrapolations provided by Robertson et al., the exponential coefficients of the best fit power−law for the two studies were 0.41 and 0.34 (Robertson et al., 2012), respectively, and both reported a fatigue limit at 10^7 cycles between 0.6% and 0.7% strain amplitudes.

Rotary bending fatigue produces an alternating tensile-compressive strain (stress) gradient that will necessarily interact with the residual stresses present in the wire due to the pre-straining process. It is expected that the tensile strains from cycling will algebraically add to the existing tensile residual stresses to decrease the acceptable strain limits. On the other hand, the effects of tensile cyclic strains may be reduced in the compressive residual regions. Furthermore, it is expected that the effects of residual stress will be most important during cycling at lower strain (and stress) amplitudes in the linear elastic regions. At strain amplitudes greater than the linear elastic limit (0.8%), stress-induced martensite will form with accompanying dislocation formation (Pelton, 2011) that may modify the existing dislocation/martensite microstructure. Cycling at these higher strains can lead to a phenomenon referred to as “residual stress fading” that would nullify any existing internal stresses. This fading is demonstrated in many engineering materials, for example, in AISI 1080 steel with a variety of heat treatments to create different levels of microstresses as well as macrostressess by shot peening (Winholtz and Cohen, 1992). X-ray diffraction was used to quantify the microstresses and macrostresses from processing and fatigue cycling in that fatigue study with two levels of stress amplitude. They observed that both initial compressive and tensile microstresses fade with fatigue and that macrostresses due to shot peening also reduce with fatigue. These explanations may support the observation in the present study that low-cycle fatigue was unaffected by the pre-straining process.

Although it is beyond the goals of this study, it is interesting to speculate what actually occurs during fully reversed cycling at strain amplitudes in both the low-cycle and high cycle regions. For example, we first consider wires with no pre-strain process. For each rotation at strain amplitudes greater than 0.8%, the wires undergo sequential tension and compression and therefore differences in the martensite variants that form. It is expected that these martensites are able to retransform to austenite upon unloading of the strain on the reverse cycle. However, as the number of cycles increase, it is likely that the accumulation of transformation plasticity may begin to stabilize the martensite creating a metastable microstructure. Monitoring these microstructures under these conditions with in situ x-ray or neutron diffraction may elucidate how continued strain cycles interact.

4.4. Strain life

In the present investigation, wires were fatigued until fracture or run out at 10^8 cycles, in part to discern whether the fatigue limit at 10^8 cycles can be effectively extrapolated from results run out to 10^7 cycles. In 0% pre-strain wires, four samples achieved run out at 10^7 cycles but only one of these wires reached 10^8 cycles at 0.6% strain amplitude. On the other hand, at 0.4% strain amplitude in 8% pre-strain wire, the four wires that withstood 10^7 cycles of loading reached run out at 10^8 cycles. In both cases, the average number of cycles to failure fell between 10^7 and 10^8 cycles. Similar results have been documented in prior high-cycle fatigue investigations. Patel and colleagues studied the effect of surface finish on 0.323mm $Ni_{50.8}Ti_{49.2}$ wires using RBF conducted to 10^8 cycles at strain levels ranging from 0.7% to 2.5% (Patel and Gordon, 2008). The A_f of the wires ranged from 18 to 24 °C, and testing was conducted at 10 °C above the A_f temperature. Though individual data points were not provided, the average fatigue life at 0.8% strain amplitude and 0.7% strain amplitude ranged from 10^7 to 10^8 for every surface finish, with at least one of seven wires tested at 0.8% strain amplitude and four of seven wires tested at 0.7% strain amplitude in each group achieving run out at 10^8 cycles. More recently, Rahim et al. investigated the effects of impurity (O, C) on the RBF properties of 0.75mm pseudoelastic Nitinol wires with $A_{f=}$30 °C (Rahim et al., 2013b). The wires were tested at 37 °C at strain levels from 0.94% and 1.88% for up to 6×10^8 cycles. The high purity material had superior fatigue properties compared to O-rich and C-rich materials in the low-cycle region, while C-rich and high purity materials had comparable fatigue resistance at higher cycles. However, notable scatter was observed in the high-cycle fatigue data, with several wires from each composition fracturing below 10^7 cycles, between 10^7 and 10^8 cycles and even between 10^8 and 6×10^8 cycles at 0.94%, 1% and 1.07% strain amplitudes. These results indicate that not all individual samples achieving run out 10^7 cycles will survive to 10^8 cycles, due in part to the stochastic nature of microstructural damage accumulation (Rahim et al., 2013b). However, as the mechanisms underlying fatigue fracture in Nitinol at 10^7 cycles are similar to those at 10^8 cycles, testing to 10^7 cycles should still provide mechanistic insights into the high-cycle and ultrahigh cycle fatigue behavior of the material.

4.5. Fractography

The shape, size and morphology of the fractured surfaces were found to be comparable between pre-strain and control wires, indicating similar mechanisms underlying fatigue fracture of the wires. In Nitinol, fatigue cracks initiate at inclusions (oxides and carbides) and other internal defects, and in most of the wires inspected in the present study, inclusions were clearly visible at the site of crack nucleation. Rahim and colleagues have recently conducted a thorough SEM analysis of the longitudinal surface of rotary bend fatigued Nitinol wires. The authors showed that more than 80% of microcracks that form around surface inclusions nucleate from inclusions with processing voids, such as the one observed in Fig. 9, rather than fully embedded inclusions (Rahim et al., 2013b). Though the exact role of these inclusions is still not fully understood, in general, it is observed that increasing purity increases the acceptable strain amplitude at 10^7−10^8 cycles (Launey et al., 2014; Rahim et al., 2013b). In the absence of other processing defects, these inclusion-associated voids should act as the site of crack initiation in low-cycle, high-cycle and even ultra-high cycle fatigue regimes, independent of exposure to pre-strain. This is in contrast to high-strength steels, where fractures at ultra-high cycles nucleate from internal defects (fish-eyes fractures) (Sakai et al., 2010).

In the present work, SEM analysis of the fractured surfaces showed that, from the site of initiation, a stable fatigue crack zone was present as a distinct thumbnail shaped region, consistent with the crack shape seen in fully reversed bending fatigue of metal wires (Stephens et al., 2000). This shape, as quantified by the ratio of maximum crack length to crack width ($a_{max}/2b_{max}$), was nearly constant across pre-strain and strain amplitude in the low-cycle regime. At 0.6% strain amplitude, however, there was a slight decrease in ($a_{max}/2b_{max}$) due to flattening of the crack growth front. Limited transformational strains are generated at this lower strain amplitude, and fatigue should largely occur within linear elastic bounds. This evolution in crack shape is consistent with computational models of linear elastic circular bars subject to cyclic bending, in which initially semi-circular (thumbnail) crack fronts gradually become linear as crack depth (a_{max}) increases (Carpinteri et al., 2006).

The size of the fatigue fracture region also increased with decreasing strain amplitude, increasing from just over 20% at 1.5% strain amplitude to 55% at 0.6%. Rahim et al. also conducted fractography of RBF wires using SEM to quantify the initial fatigue crack area as a function of fatigue strain (Rahim et al., 2013a). They found that crack area monotonically increased from approximately 23% at 1.88% strain amplitude to 47% at 0.94% strain amplitude. As such, with decreasing strain amplitude the fatigue crack can consume up to half of the fracture surface before final tensile overload.

In contrast, for a given strain amplitude, the fatigue crack area was similar between pre-strain levels, even in wires with vastly different fatigue life. As has been previously suggested (Robertson et al., 2012), and recently quantified, this indicates that the majority of fatigue life is associated with crack initiation, with limited stable crack growth prior to failure due to the small cross-sectional area of the wires. Using the fatigue striations present in SEM images of the fracture surfaces of RBF tested wires, Rahim and colleagues quantified the percentage of fatigue life spent in crack initiation versus crack propagation (Rahim et al., 2013b). At larger strain amplitudes, they found that 25% or more of fatigue life may be consumed with stable crack growth. In contrast, over 95% of cycles to failure at lower strain amplitudes were associated with crack initiation. Since crack initiation occurs at surface inclusions, pre-strain-induced plasticity, which is concentrated in the outer fibers, may serve to accelerate the formation/initiation of flaws from these inclusions, thereby preferentially reducing the high-cycle fatigue life of the pre-strained wires.

The surface morphology of the fatigue crack zone and the zone of ductile fracture were independent of both strain amplitude and pre-strain levels. Previous RBT studies of pseudoelastic Nitinol wires over a range of alternating strains have observed surface morphologies similar to those seen here (Patel et al., 2006; Schaffer and Plumley, 2009), and have also found that the morphology of the fatigue fracture zone remains the same between low- and high-cycle fatigue regimes (Pelton et al., 2013; Weaver et al., 2013). As noted above, changes in microstructure due to pre-straining are concentrated along the outer wire fibers, so differences in fracture surface morphology between 0%, 8% and 10% prestrain wires should be limited to a small zone around the site of crack initiation. Further, since fatigue crack propagation in Nitinol takes place through the formation of deformed martensite (Robertson et al., 2007; Stebner et al., 2013), irrespective of the phase of material, the morphology of both the fatigue fracture surface and the ductile overload surface are expected to be similar across pre-strain levels.

4.6. Limitations

Though the strain amplitudes employed in the current study are representative of the cyclic strains to which devices are exposed in vivo during pulsatile and musculoskeletal loading, rotary bend fatigue experiments do not capture the effects of mean strain/stress. Material- and device-level mean strains from 2% to 6% have been observed to enhance the fatigue life Nitinol (Morgan et al., 2004; Pelton et al., 2008; Tabanli et al., 1999), with cycling within the transformation regime thought to confer aprotective benefit against fatigue failure. While the presence of mean strain may offer some additional damage resistance, we anticipate that mean strain alone would not completely mitigate the effects of the pre-strain-induced damage seen here, and that the trends observed herein would remain.

Due to the constraints of the experimental set-up, loading in the present study was limited to pure bending. However, rather than pure bending, endovascular devices are exposed to complex multi-axial loads in vivo. While the current results show that large bending pre-strains negatively affect bending fatigue properties, and indirectly, that compressive pre-strains may adversely impact tensile fatigue, these finding may not necessarily translate to other deformation modes. Since the martensite variants activated in Nitinol are dependent on texture and applied load, the effects of pre-strain are anticipated to be a function of material processing and both pre-strain mode and deformation mode. In fact, preliminary evidence suggests that tensile pre-strains may actually improve the tension−tension fatigue properties of Nitinol. For example, Launey and colleagues have recently conducted tension−tension fatigue studies of pseudoelastic wires (A_f=20 °C) at 37 °C with pre-strain values of 6%, 7.5%, 9% and 10.5%. They observe that the 10^7-cycle fatigue strain limit at 3% mean strain monotonically increases from 0.27% (6%), to 0.33% (7.5%), to 0.39% (9.0%), to 0.48% (10.5%) (personal communication). It is speculated that the beneficial effects of tensile pre-strain are due to compressive residuals upon unloading as well as favorable martensite variants for subsequent fatigue cycling. The effects of pre-straining and strain portioning as described in this paper can only be fully ascertained through extensive in situ micro-XRD and TEM studies. These authors intend to explore these microstructural factors in an upcoming paper.

5. Conclusions

The present work represents an important step towards elucidating the effects of thermo-mechanical pre-strains on the fatigue properties of Nitinol. This study investigated the rotary bend fatigue characteristics of pseudoelastic Nitinol wires subjected to large bending pre-strains under zero mean strain conditions at 37 °C across a range of physiologic strain amplitudes. The results show that bending pre-strains in excess of 8% produce a pronounced residual set in Nitinol wires. Due to the load and texture-dependent formation of martensite variants, which leads to tension−compression asymmetry in Nitinol, this prestrain-induced residual set is thought to be associated with non-uniform plasticity, retained deformed martensite and residual stresses that are preferentially distributed along the compressive pre-strain surface.

Consequently, even though the highest strains in the pre-strained wires are concentrated along a small volume of material within the outer fibers, they serve to accelerate crack initiation along the compressive surface, thereby significantly reducing the fatigue life of the wires, even at strain amplitude as low as 0.3%. This suggests that even if only a small volume of the total material in an endovascular implant undergoes significant compressive deformation during crimping, sterilization and deployment, the pre-strained regions are more susceptible to fracture under tensile loading, even at the small strain amplitudes imposed by in vivo pulsatile loads. Further, identifying these regions of high strain may help reconcile some of the discrepancies observed between finite element analyses, benchtop testing and clinical performance of these implants.

In contrast to fatigue life, the mechanisms underlying fatigue failure are not influenced by pre-strain; at the strain amplitudes sampled in the present study, fatigue cracks initiate from processing voids surrounding inclusions, and fatigue fracture surfaces are comprised of characteristic regions of crack initiation and stable growth and ductile tensile overload. These mechanisms are largely constant, irrespective of the number of cycles to failure, suggesting that though experimental work in the medium to high-cycle regime may not necessarily provide a quantitative fatigue limit, it can still be used to glean mechanistic insights into very high-cycle fatigue behavior of the material.

Further research is necessary to understand more fully the effects of different types of pre-strain on the fatigue properties of Nitinol under a variety of deformation modes. Nevertheless, the sensitivity of the material to compressive-pre-strain induced damage and the resulting reduction in fatigue life highlight the importance of incorporating thermo-mechanical history into the design and testing of wire-based percutaneous devices such as endovascular grafts and occluders, particularly as smaller catheters and greater pre-strains are adopted for device delivery.

Acknowledgments

The authors would like to acknowledge support from the FDA Commissioner’s Fellowship Program. Nitinol wires were provided by Nitinol Devices and Components through a materials transfer agreement. We would like to thank Lot Vien for assistance with electropolished wire fabrication, Jason Galginaitis and Timothy Murphy for their assistance with fatigue testing and SEM analysis, Hamed Ghods and Glenn Link for modifying RBT systems. We also acknowledge stimulating conversations with Professor Aaron Stebner (Colorado School of Mines).

REFERENCES

Bannantine JA, Comer JJ, Handrock JL, 1990 Fundamentals of Metal Fatigue Analysis. Prentice Hall, Saddle River, NJ.

Barney MM, Xu D, Robertson SW, Schroeder V, Ritchie RO, Pelton AR, Mehta A, 2011 Impact of thermomechanical texture on the superelastic response of Nitinol implants. J. Mech. Behav. Biomed. Mater 4, 1431–1439 [PubMed: 21783153]

Berg BT, 1995 Bending of Superelastic Wires. 1. Experimental Aspects. J. Appl. Mech.—Trans. ASME 62, 459–465.

Bhattacharya K, 2003 Microstructure of Martensite: Why it Forms and How it Gives Rise to the Shape-Memory Effect.Oxford University Press, Oxford.

Brinson LC, Schmidt I, Lammering R, 2004 Stress-induced transformation behavior of a polycrystalline NiTi shape memory alloy: micro and macromechanical investigations via in situ optical microscopy. J. Mech. Phys. Solids 52, 1549–1571.

Carpinteri A, Brighenti R, Vantadori S, 2006 Surface cracks in notched round bars under cyclic tension and bending. Int. J. Fatigue 28, 251–260.

Chinubhai A, Kueck A, Saffari P, Senthilnathan K, Vien L, Pelton AR, 2013 A.S.M. International. Factors causing compressive damage-induced cracking in Nitinol. Med. Dev. Mater. Vi, 139–142.

Duerig T, Pelton A, Stockel D, 1999 An overview of Nitinol medical applications. Mater. Sci. Eng. A A273−275, 149–160

Duerig TM, Melton KN, Stockel D, Wayman CM, 1990 Engineering Aspects of Shape Memory Alloys. Butterworth-Heinemann, London.

Fagan T, Dreher D, Cutright W, Jacobson J, Latson L, Working GHSO, 2009 Fracture of the GORE HELEX septal occluder: associated factors and clinical outcomes. Catheter. Cardiovasc. Interv 73, 941–948. [PubMed: 19213077]

Gall K, Sehitoglu H, 1999 The role of texture in tension-compression asymmetry in polycrystalline NiTi. Int. J. Plast 15, 69–92.

Gall K, Sehitoglu H, Chumlyakov YI, Kireeva IV, 1999 Tension−ompression asymmetry of the stress-strain response in aged single crystal and polycrystalline NiTi. Acta Mater. 47, 1203–1217.

Gong JM, Tobushi H, Takata K, Okumura K, 2002 Superelastic deformation of a TiNi shape memory alloy subjected to various cyclic loadings. Proc. Inst. Mech. Eng. Part L—J. Mater.—Des. Appl 216, 17–23.

Grujicic M, Pandurangan B, Arakere A, Snipes JS, 2012 Fatigue-life computational analysis for the self-expanding endovascular Nitinol stents. J. Mater. Eng. Perform 21, 2218–2230.

Henderson E, Nash DH, Dempster WM, 2011 On the experimental testing of fine Nitinol wires for medical devices. J. Mechan. Behav.f Biomed. Mater 4, 261–268.

Jacobus K, Sehitoglu H, Balzer M, 1996 Effect of stress state on the stress-induced martensitic transformation in polycrystalline Ni−Ti alloy. Metall. Mater. Trans. A—Phys. Metall. Mater. Sci 27, 3066–3073.

James B, et al. (2004). Compressive Damage-Induced Cracking in Nitinol. Proceedings of the International Conference on Shape Memory and Superelastic Technologies Baden-Baden, Germany SMST: 117–124.

Kay JD, O'Laughlin MP, Ito K, Wang A, Bashore TM, Harrison JK, 2004 Five-year clinical and echocardiographic evaluation of the Das AngelWings atrial septal occluder. Am. Heart J 147, 361–368. [PubMed: 14760337]

Kleinstreuer C, Li Z, Basciano CA, Seelecke S, Farber MA, 2008 Computational mechanics of Nitinol stent grafts. J. Biomech 41, 2370–2378. [PubMed: 18644312]

Kumar GP, Cui FS, Danpinid A, Su BY, Hon JKF, Leo HL, 2013 Design and finite element-based fatigue prediction of a new self-expandable percutaneous mitral valve stent. Comput.-Aided Des 45, 1153–1158.

Kumar GP, Mathew L, 2012 Self-expanding aortic valve stent— material optimization. Comput. Biol. Med 42, 1060–1063. [PubMed: 22981766]

Launey M, Robertson SW, Vien L, Senthilnathan K, Chintapalli P, Pelton AR, 2014 Influence of microstructural purity on the bending fatigue behavior of VAR-melted superelastic Nitinol. J. Mech. Behav. Biomed. Mater 34, 181–186. [PubMed: 24603214]

Matheus T, Menezes W, Rigo O, Kabayama L, Viana C, Otubo J, 2011 The influence of carbon content of cyclic fatigue of NiTi SMA wires. Int. Endod. J 44, 567–573. [PubMed: 21314829]

Matsumoto O, Miyazaki S, Otsuka K, Tamura H, 1987 Crystallography of martensitic-transformation in Ti−Ni crystals. Acta Metall. 35, 2137–2144.

Miyazaki S, Igo Y, Otsuka K, 1986 Effect of thermal cycling on the transformation temperatures of Ti−Ni alloys. Acta Metall. 34, 2045–2051.

Miyazaki S, Kimura S, Otsuka K, Suzuki Y, 1984 The habit plane and transformation strains associated with the martensitic-transformation in Ti−Ni single crystals. Scr. Metall 18, 883–888.

Morgan NB, Painter J, Moffat A, 2004 Mean strain effects and microstructural observations during in vitro fatigue testing of NiTi. SMST - Proceedings on International Conference on Shape Memory and Superelastic Technologies, Pacific Grove, CA, pp. 303–310.

Nikanorov A, Smouse HB, Osman K, Bialas M, Shrivastava S, Schwartz LB, 2008 Fracture of self-expanding nitinol stents stressed in vitro under simulated intravascular conditions. J. Vasc. Surg 48, 435–440. [PubMed: 18486426]

Norwich DW, 2014 A comparison of zero mean strain rotating beam fatigue test methods for Nitinol wire. J. Mater. Eng. Perform 23, 2515–2522.

Norwich DW, Fasching A, 2009 A study of the effect of diameter on the fatigue properties of NiTi wire. J. Mater. Eng. Perform 18, 558–562.

Oppenheimer SM, Yung AR, Dunand DC, 2007 Power-Law Creep in Near-Equiatomic Nickel-Titanium Alloys. Scripta Materialia 57, 377–380.

Otsuka K, Ren X, 2005 Physical metallurgy of Ti−Ni-based shape memory alloys. Prog. Mater. Sci 50, 511–678.

Patel M, Plumley D, Bouthot R, Proft J, 2006 The effects of varying active af temperatures on the fatigue properties of nitinol wire. In: Venugopalan R, Wu M (Eds.), Medical Device Materials III: Proceedings from the Materials & Processes for Medical Devices Conference 2005, pp. 148–153.

Patel MM, Gordon RF, 2008 An investigation of diverse surface finishes on fatigue properties of superelastic Nitinol wire. In: Berg B, Mitchell MR, Proft J (Eds.), SMST 2006: Proceedings of the International Conference on Shape Memory and Superelastic Technologies, pp. 61–70.

Pelton AR, 2011 Nitinol fatigue: a review of microstructures and mechanisms. J. Mater. Eng. Perform 20, 613–617.

Pelton AR, DiCello J, Miyazaki S, 2000 Optimisation of processing and properties of medical grade Nitinol wire. Minim. Invasive Ther. Allied Technol 9, 107–118.

Pelton AR, Duerig TW, Stockel D, 2004 A guide to shape memory and superelasticity in Nitinol medical devices. Minim. Invasive Ther. Allied Technol 13, 218–221. [PubMed: 16754129]

Pelton AR, Fino-Decker J, Vien L, Bonsignore C, Saffari P, Launey M, Mitchell MR, 2013 Rotary-bending fatigue characteristics of medical-grade Nitinol wire. J. Mech. Behav. Biomed. Mater 27, 19–32. [PubMed: 23838356]

Pelton AR, Huang GH, Moine P, Sinclair R, 2012 Effects of thermal cycling on microstructure and properties in Nitinol. Mater. Sci. Eng. A—Struct. Mater. Prop. Microstruct. Process 532, 130–138.

Pelton AR, Russell SM, DiCello J, 2003 The physical metallurgy of Nitinol for medical applications. J. Miner. Met. Mater. Soc 55, 33–37.

Pelton AR, Schroeder V, Mitchell MR, Gong XY, Barney M, Robertson SW, 2008 Fatigue and durability of Nitinol stents. J. Mech. Behav. Biomed. Mater 1, 153–164. [PubMed: 19627780]

Plietsch R, Ehrlich K, 1997 Strength differential effect in pseudoelastic NiTi shape memory alloys. Acta Mater. 45, 2417–2424.

Rahim M, Frenzel J, Frotscher M, Heuwer B, Hiebeler J, Eggeler G, 2013a Bending rotation HCF testing of pseudoelastic Ni−Ti shape memory alloys. Mater. Werkst 44, 633–640.

Rahim M, Frenzel J, Frotscher M, Pfetzing-Micklich J, Steegmuller R, Wohlschlogel M, Mughrabi H, Eggeler G, 2013b Impurity levels and fatigue lives of pseudoelastic NiTi shape memory alloys. Acta Mater. 61, 3667–3686.

Rebelo N, Fu R, Lawrenchuk M, 2009 Study of a Nitinol stent deployed into anatomically accurate artery geometry and subjected to realistic service loading. J. Mater. Eng. Perform 18, 655–663.

Reedlunn B, Churchill CB, Nelson EE, Shaw JA, Daly SH, 2014 Tension, compression, and bending of superelastic shape memory alloy tubes. J. Mech. Phys. Solids 63, 506–537.

Reinoehl M, Bradley D, Bouthot R, Proft J, 2001 The influence of melt practice on final fatigue properties of superelastic NiTi wires, In: Russell SM, Pelton AR (Eds.), 2000 SMST −

Proceedings on International Conference on Shape Memory and Superelastic Technologies Pacific Grove, CA, pp. 397–403.

Robertson SW, Gong XY, Ritchie RO, 2006 Effect of product form and heat treatment on the crystallographic texture of austenitic Nitinol. J. Mater. Sci 41, 621–630.

Robertson SW, Mehta A, Pelton AR, Ritchie RO, 2007 Evolution of crack-tip transformation zones in superelastic Nitinol subjected to in situ fatigue: a fracture mechanics and synchrotron X-ray microdiffraction analysis. Acta Mater. 55, 6198–6207.

Robertson SW, Pelton AR, Ritchie RO, 2012 Mechanical fatigue and fracture of Nitinol. Int. Mater. Rev 57, 1–36.

Sakai T, Lian B, Takeda M, Shiozawa K, Oguma N, Ochi Y, Nakajima M, Nakamura T, 2010 Statistical duplex S−N characteristics of high carbon chromium bearing steel in rotating bending in very high cycle regime. Int. J. Fatigue 32, 497–504.

Schaffer JE, Plumley DL, 2009 Fatigue performance of nitinol round wire with varying cold work reductions. J. Mater. Eng. Perform 18, 563–568.

Schlun M, Zipse A, Dreher G, Rebelo N, 2011 Effects of cyclic loading on the uniaxial behavior of Nitinol. J. Mater. Eng. Perform 20, 684–687.

Shaw JA, Kyriakides S, 1995 Thermomechanical aspects of NiTi. J. Mech. Phys. Solids 43, 1243–1281.

Sheriff J, Pelton AR, Pruitt LA, 2005 Hydrogen effects on nitinol fatigue. In: Helmus M, Medlin D (Eds.), Medical Device Materials II: Proceedings from the Materials & Processes for Medical Devices Conference 2004, pp. 38–43.

Shimizu K, Tadaki T, 1984 Shape Memory Alloys. Gordon and Breach.

Stebner AP, Vogel SC, Noebe RD, Sisneros TA, Clausen B, Brown DW, Garg A, Brinson LC, 2013 Micromechanical quantification of elastic, twinning, and slip strain partitioning exhibited by polycrystalline, monoclinic nickel−titanium during large uniaxial deformations measured via in-situ neutron diffraction. J. Mech. Phys. Solids 61, 2302–2330.

Stephens RI, Fatemi A, Stephens RR, Fuchs HO, 2000 Metal Fatigue in Engineering, 2nd ed. John Wiley & Sons, Inc., New York.

Tabanli RM, Simha NK, Berg BT, 1999 Mean stress effects on fatigue of NiTi. Mater. Sci. Eng. A—Struct. Mater. Prop. Microstruct. Process 273, 644–648.

Trabattoni D, Agrifoglio M, Cappai A, Bartorelli AL, 2010 Incidence of stent fractures and patency after femoropopliteal stenting with the nitinol self-expandable SMART stent: a single-center study. J. Cardiovasc. Med 11, 678–682.

Urbina C, De la Flor S, Ferrando F, 2009 Effect of thermal cycling on the thermomechanical behaviour of NiTi shape memory alloys. Mater. Sci. Eng. A—Struct. Mater. Prop. Microstruct. Process 501, 197–206.

Weaver J, Gupta S, Woods T, 2013 Effects of test speed on fatigue life of Nitinol wire in rotary bend In: Mitchell MR, Smith SW, Woods T, Berg BT (Eds.), Fatigue and Fracture of Medical Metallic Materials and Devices, 1559. STP, West Conshohocken, PA, pp. 1–17.

Wick A, Gong XY, Fino J, Sheriff J, Pelton AR, 2005 Bending fatigue characteristics of nitinol. Medical Device Materials II: Proceedings from the Materials & Processes for Medical Devices Conference 2004, pp. Minneapolis, MN, pp. 15–20.

Winholtz RA, Cohen JB, 1992 Changes in the macrostresses and microstresses in steel with fatigue. Mater. Sci. Eng. A—Struct. Mater. Prop. Microstruct. Process 154, 155–163.

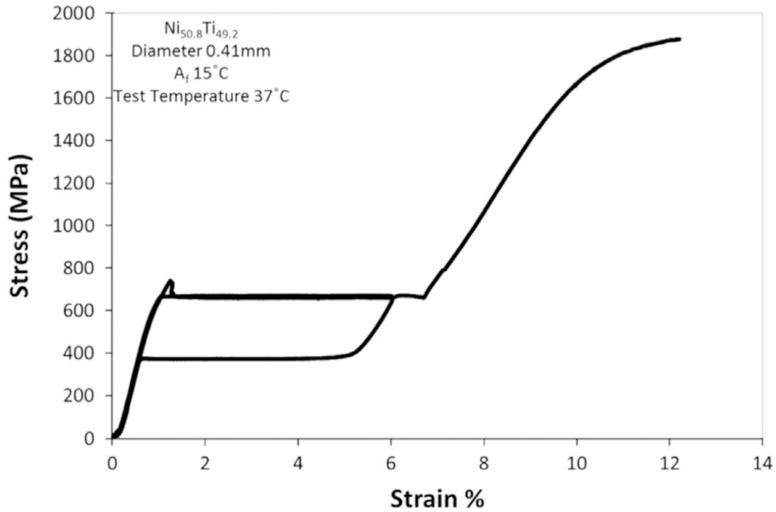

Fig. 1 −.

Uniaxial tensile stress−strain behavior of $Ni_{50.8}Ti_{49.2}$ wire with A_f=15 °C used in the RBT testing. Tensile testing was performed in accordance with ASTM F2516 at 37 °C.

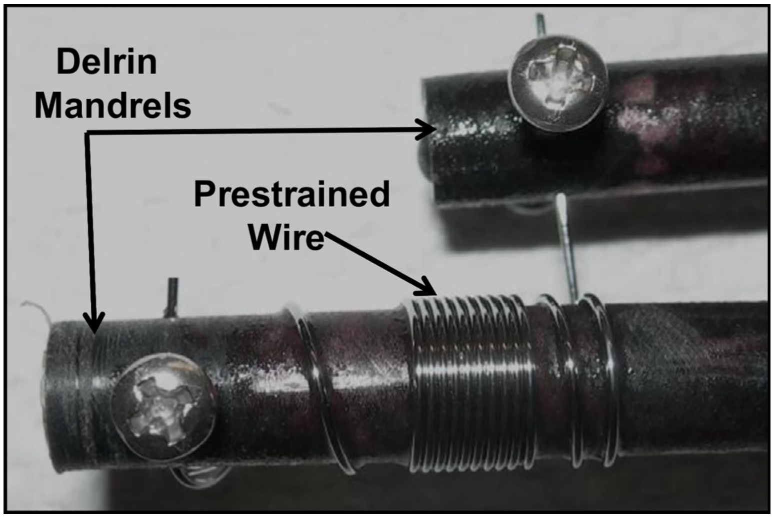

Fig. 2 –.

Representative photograph of Nitinol wires wrapped around delrin mandrels during the pre-strain process. The wires are wrapped into this configuration while they are immersed in a 0 °C water bath. The wire-mandrel combination is subsequently placed into 60 °C and RT baths before the wires are released from the mandrels.

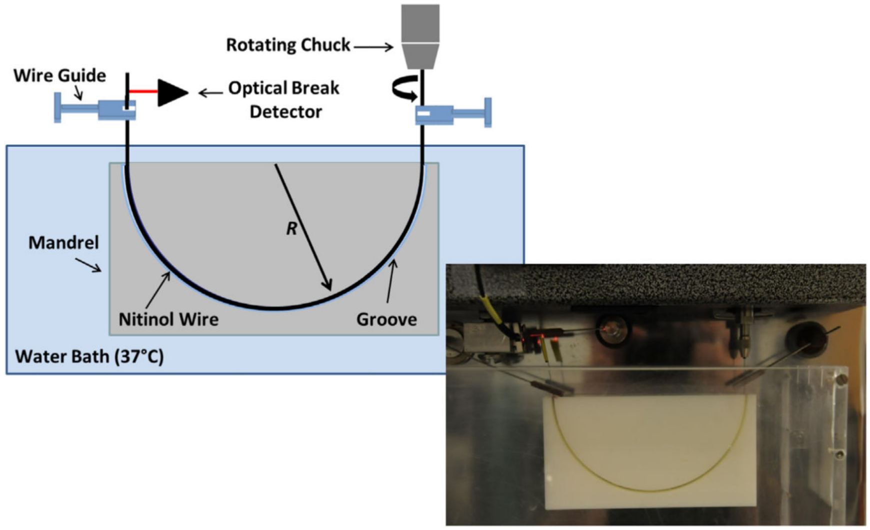

Fig. 3 –.

Schematic and photograph of the modified rotary bend fatigue test set-up. The complete Valley Instruments System electronics have not been illustrated.

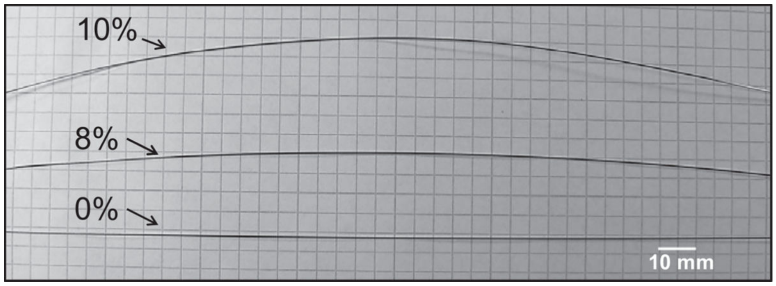

Fig. 4 −.
Representative photograph of the remnant set present in 0% (bottom) 8% (middle) and 10% (top) Nitinol wires after thermo-mechanical pre-straining. While clearly visible in both 8% and 10% wires, the remnant set is more pronounced in 10% pre-strain wires.

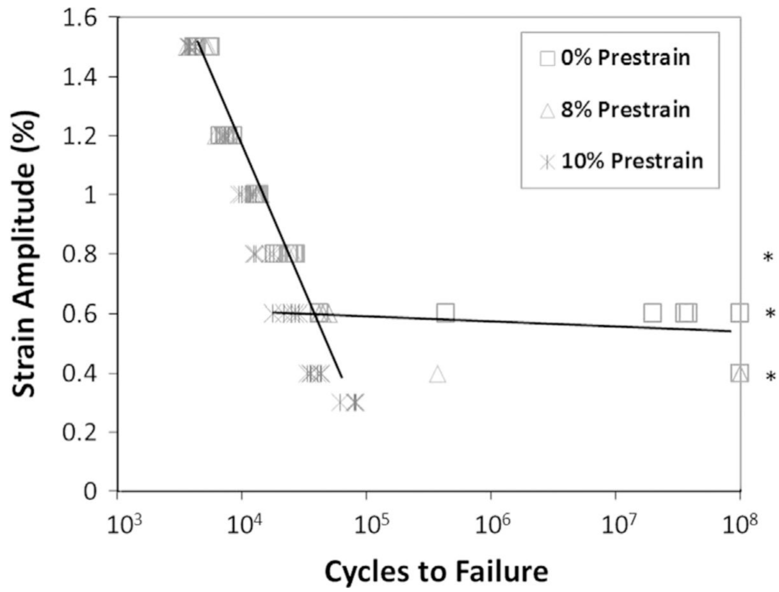

Fig. 5 –.

Strain amplitude versus number-of-cycles curve for 0%, 8% and 10% pre-strain Nitinol wires tested at strain amplitudes from 1.5% to 0.3%. Data points at 10^8 cycles represent samples that did not fracture. The curves for 0% and 8% prestain wire exhibit distinct low-cycle and high-cycle fatigue regions (delineated by trend lines). In the low-cycle region, fatigue life is comparable across pre-strain levels, but diverges significantly at strain amplitudes ≤0.8%.

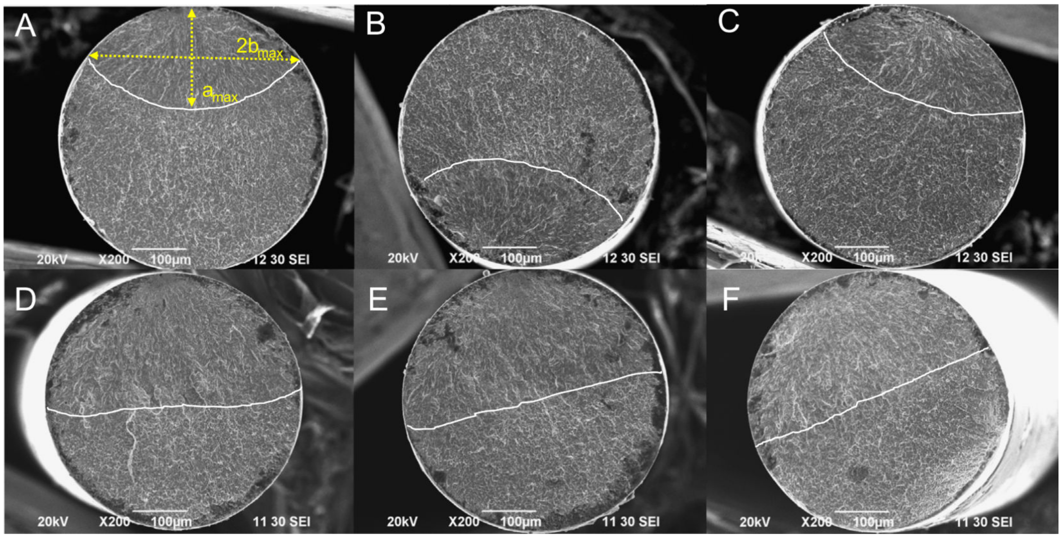

Fig. 6 –.

SEM images of fracture surfaces for wire tested at 1.2% strain amplitude for (a) 0% pre-strain (7.3×10^3 cycles) (b) 8% pre-strain (8.0×10^3 cycles) (c) 10% pre-strain (6.9×10^3 cycles) wires. SEM images of fracture surfaces for wire tested at 0.6% strain amplitude for (d) 0% pre-strain (3.6×10^7 cycles) (e) 8% pre-strain (4.5×10^4 cycles) (f) 10% pre-strain (2.9×10^4 cycles) wires. Each wire had two distinct regions, and the size and morphology of these regions was similar across pre-strain levels, despite large differences in cycles to failure.

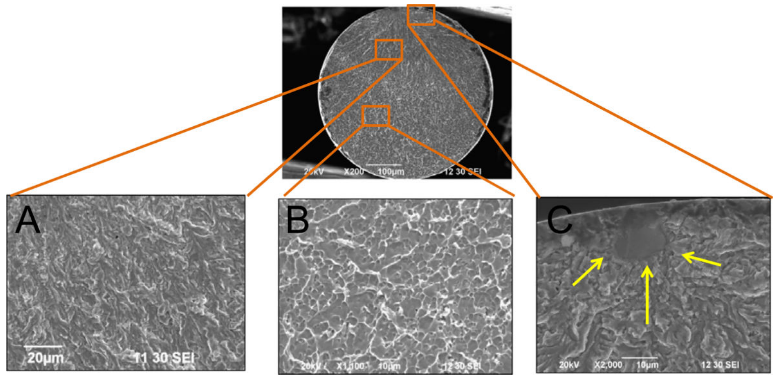

Fig. 7 –.

Magnified SEM images of the fractured surfaces. Each wire had two distinct regions, (a) a thumbnail shaped region of fatigue crack growth and (b) a region of ductile tensile overload. (c) Within the region of fatigue crack growth, cracks were observed to initiate from surface inclusions.

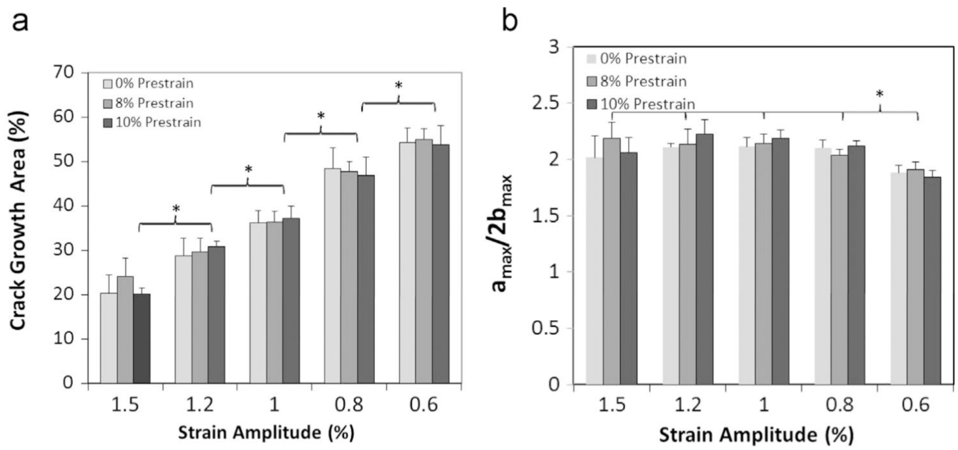

Fig. 8 –.

Changes in (a) fatigue fracture area and (b) crack shape of fracture surfaces with strain amplitude and pre-strain level. Both parameters were similar across pre-strain levels, irrespective of strain amplitude. While fatigue fracture area increased significantly increasing strain amplitude, crack shape was similar for all strain amplitudes ≥0.8%.

Author Manuscript

Author Manuscript

Author Manuscript

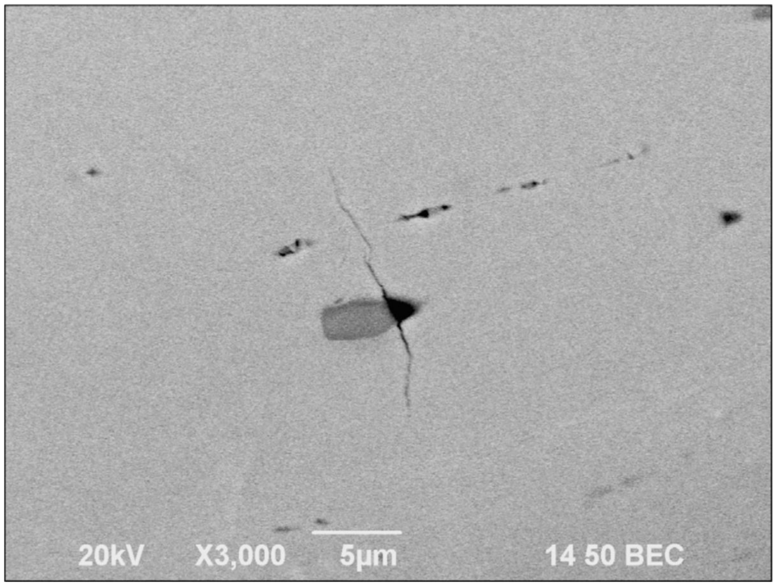

Fig. 9 −.

BEI image of a microcrack originating and propagating from an inclusion-associated void observed along the longitudinal (circumferential) surface of a 10% prestrain wire tested at 1.0% strain amplitude (1.3×10^4 cycles to failure).

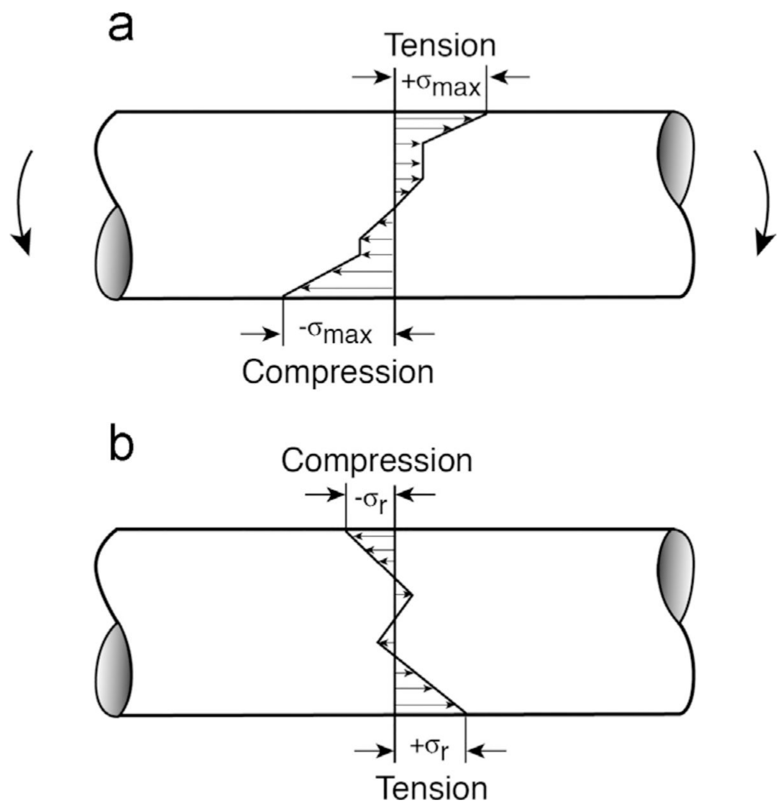

Fig. 10 −.
(a) Schematic illustration of the stress distribution across the wire during the pre-straining process. (b) Potential tension−compression redistribution for the unconstrained wires after pre-straining (Adopted from Bannantine).

Author Manuscript

Author Manuscript

Author Manuscript

Table 1 –

Number of wires tested at each experimental pre-strain and alternating strain level.

Alternating strain (%)	Pre-strain level (%)		
	0%	**8%**	**10%**
1.5	5	6	6
1.2	5	5	5
1.0	5	5	5
0.8	5	5	5
0.6	6	6	6
0.4	6	5	6
0.3	-	-	5

Table 2 –

Residual strain in pre-strained wire before and after heating above M_d.

Sample	Residual strain (%)			
	8% Pre-strain		10% Pre-strain	
	Before	After	Before	After
1	0.026 ± 0.014	0.022 ± 0.02	0.075 ± 0.026	0.058 ± 0.03
2	0.036 ± 0.026	0.024 ± 0.018	0.061 ± 0.034	0.054 ± 0.041

Table 3 –

Location of fatigue crack initiation relative to applied prestain.

Alternating strain (%)	Location					
	8% Prestrain			10% Prestrain		
	Compressive	Neutral	Tensile	Compressive	Neutral	Tensile
1.5	3/6	3/6	0/6	4/6	1/6	1/6
1.2	4/5	0/5	1/5	4/5	1/5	0/5
1.0	5/5	0/5	0/5	5/5	0/5	0/5
0.8	4/5	0/5	1/5	2/5	1/5	2/5
0.6	5/6	1/6	0/6	3/6	3/6	0/6
0.4	1/5	0/5	0/5	4/6	1/6	1/6